Phase behaviour of poly(2, 6-diphenyl-p-phenylene oxide) (PPPO) in mixed solvents

Róisín A. O'Connell[a], Alexandra E. Porter[b], Julia S. Higgins[a], João T. Cabral[a,*]

[a]Department of Chemical Engineering, Imperial College London, South Kensington, London, United Kingdom SW7 2AZ
[b]Department of Materials, Imperial College London, South Kensington, London, United Kingdom, SW7 2AZ

Abstract

The solution phase behaviour of poly(2, 6-diphenyl-p-phenylene oxide) (PPPO) is investigated by a combination of turbidimetry, infrared spectroscopy, dynamic light scattering and densitometry, combined with calorimetry and X-ray scattering. We select dichloromethane (DCM) and heptane as, respectively, representative good and poor solvents for the polymer. This ternary system results in a miscibility gap which can be utilised for the design and fabrication of PPPO porous materials, membranes and scaffolds *via* phase inversion. We establish the phase diagram and resolve the kinetic solidification condition arising from the intersection between the coexistence and glass transition curves. PPPO exhibits a high $T_g \approx 230\ °C$ and is found to crystallise at $T_c \approx 336\ °C$, and melt at $T_m \approx 423, 445\ °C$ with a double endotherm. The kinetics of demixing and (buoyancy-driven) stratification are quantified by optical imaging and the PPPO-rich phase analysed by SAXS/WAXS to resolve both amorphous and crystalline phases. Equipped with this knowledge, we demonstrate the controlled formation of nodular, bicontinuous and cellular morphologies by non-solvent induced demixing.

Keywords: phase behaviour, crystallisation, demixing, porous materials

1. Introduction

Liquid-liquid demixing, generally accompanied by phase inversion and solidification, is a versatile route to generating membranes, scaffolds and porous polymer materials [1, 2]. This ubiquitous process exploits the phase behaviour of a polymer blend or solution, most commonly by changing the temperature of the system (thermally induced phase separation, TIPS) or by addition of a poor solvent (nonsolvent induced phase separation, NIPS) [3]. Demixing results in two phases, a polymer-rich phase that eventually forms the matrix of the material and a polymer lean phase, which forms the void structure [4].

NIPS is often rationalised in terms of the Flory-Huggins theory for ternary polymer/solvent/nonsolvent systems [5]. Demixing occurs at an elevated free energy state of the system proceeding *via* either nucleation and growth (N&G), resulting in a morphology containing droplets of polymer-poor solution dispersed within a polymer-rich matrix phase (or vice-versa), or *via* spinodal decomposition (SD) mechanisms, yielding characteristic bicontinuous interpenetrating structures, which can eventually also coarsen into a droplets (phase inversion generally occurs if the matrix is the polymer-poor phase). In each case, solidification of the polymer-rich phase can occur *via* several kinetic arrest processes; these include glass formation (upon cooling or crossing the glass transition), crystallisation, gelation or merely precipitation, allowing the solvent-rich phase to be evaporated or extracted, yielding the desired porous polymer material [5].

The thermodynamics and phase behaviour of the specific ternary system dictates the demixing pathway and the spatio-temporal evolution of the morphology until kinetic arrest. Various factors can thus affect the final porous polymer structure formed *via* NIPS, which are systematically explored in the design and fabrication of membranes and scaffolds *via* phase inversion [3]. For example, membrane flux and selectivity is (somewhat empirically) tuned by initial polymer concentration [6], molecular weight [7], relative miscibility and composition of solvent to nonsolvent(s) [8–10] additives [7], temperature and geometry of film formation and precipitation [11].

In this work, we select poly(2,6-diphenyl-p-phenylene oxide) (PPPO), with dichloromethane (DCM, good solvent) and heptane (H, nonsolvent), as a model system for NIPS. PPPO is selected due to its exceptionally high glass transition and degradation temperatures, as discussed below.

1.1. Properties of poly(2,6-diphenyl-p-phenylene oxide) (PPPO)

The monomer structure of PPPO is shown in figure 1(a). Molecular weight (M_W) of the polymer can vary; it has been synthesised in the range of 140 - 1450 kg/mol [12–14], with a fairly narrow polydispersity index (M_W/M_n) ranging from 1.4 to 2.3 [12]. It was first patented by General Electric Company in 1969 [15, 16] with the intention of its use as a synthetic paper for extra-high voltage (EHV) cables and other electronic devices, given its low relative permittivity (2.76) and dissipation factor (tan δ) of 2.5 x 10^{-4} (both values reported in air at 20 °C) [17]. PPPO was found to preferentially form unoriented crystallites upon cooling due to its bulky phenyl substituted side groups, making it brittle and difficult to mold into desirable ob-
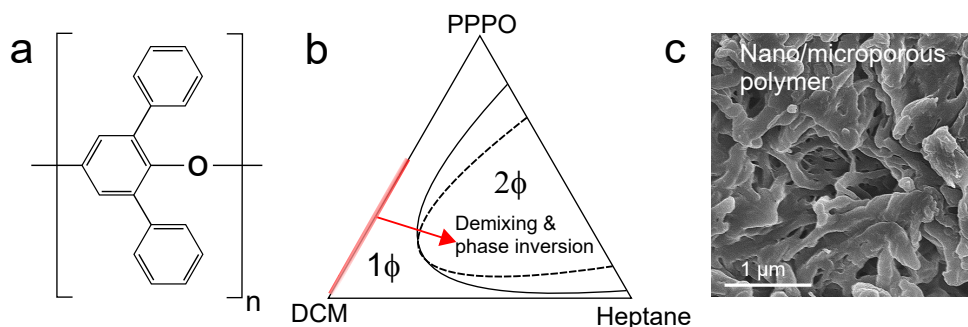

Figure 1: (a) Monomer structure of poly(2, 6-diphenyl-p-phenylene oxide) (PPPO). (b) Schematic ternary phase diagram of PPPO/dichloromethane (DCM)/heptane (see text) indicating (in red) a demixing and phase inversion pathway from a one-phase binary solution PPPO/DCM into the two-phase region by addition of heptane. (c) SEM image of porous PPPO.

jects [18, 19]. Therefore, it was further developed by AKZO Research Laboratories (formerly AKU) in the Netherlands [20], finding a range of practical applications [21–27] whose efficacy is not adversely impacted by crystallisation [28, 29].

The crystal structure of PPPO was characterised in detail by Boon and Magre [30]. Two crystal modifications were found, α and β, the former produced from melt or solution, and the latter produced only by crystallisation from solution, with the suggestion that the final structure comprises polymer and solvent molecules. The unit cell of the α polymorph is tetragonal (a = b = 12.51 Å and c = 17.08 Å), and contains eight monomeric units from two polymeric chains that run through the cell with a helical conformation [30]. It is likely the high crystal content in PPPO (up to 52% [14]) can be credited for some of the properties of PPPO that increase it functionality. For example, PPPO exhibits high thermal stability, reported between 430 and 564 °C [14, 15, 31, 32]. The degradation temperature of PPPO depends on the selected atmosphere (PPPO degrades more readily in air).

The glass transition temperature (T_g) of PPPO is found in the range of 210-240 °C, and melting temperature is generally agreed to be between 480-500 °C [14–17]. Wrasidlo [14] investigated the effect of furnace temperature and heating rate on crystallisation temperature and crystal fraction of PPPO, reporting crystal formation at temperatures between 250-450 °C. One particularly noteworthy data set shows a DSC thermogram with a crystallisation peak at 308 °C and a double endotherm melting peak at 421 and 435 °C, suggesting the presence of two crystal modifications. This was attributed to the increased cooling rate - 5 °C/min as opposed to the 0.5 °C/min used for other samples.

For the NIPS study, we consider that PPPO is largely miscible with chlorinated and aromatic solvents [17]. Thus, we select dichloromethane (DCM), as a good solvent for the ternary system. The nonsolvent heptane (H), is selected as it is largely immiscible with PPPO. DCM and heptane are fully miscible. We illustrate a schematic of the expected ternary phase diagram in figure 1(b). The arrow indicates a solvent-induced jump from the homogeneous region (in this case from a binary PPPO:DCM solution) into the two-phase region by addition of heptane. This paper seeks to systematically map the phase diagram of this ternary system, and establish pathways for demixing and struc-

ture formation of PPPO-based materials (such as displayed in figure 1(c)).

2. Experimental procedure

2.1. System

Poly(2, 6-diphenyl-p-phenylene oxide) (PPPO) (M_n = 176 kg/mol, M_w/M_n = 1.95, T_g = 228 °C). Dichloromethane (DCM, VWR Chemicals, 99.9%, ρ = 1.33 g/cm^3, refractive index = 1.424 at 20 °C [33]) and heptane (VWR Chemicals, 99.8%, ρ = 0.67 g/cm^3, refractive index = 1.385 at 20 °C [33]) were used as solvent and nonsolvent respectively. Ternary solutions were prepared gravimetrically.

2.2. Preparation of PPPO films

Polymer films were prepared by drop casting PPPO/DCM solution on glass and allowing the DCM to evaporate under ambient conditions. Films containing solvent were prepared by weighing the initial dropcast film and allowing DCM to evaporate until a desired concentration was reached. Fully dry polymer films were obtained by vacuum drying at 45 °C for 2 days. Selected films were then annealed in a Gero Carbolite furnace at 400 °C under a nitrogen atmosphere for various annealing times (1h, 2h and 4h). Samples were then analysed by DSC and WAXS, as detailed below. Phase inverted films were prepared by drop casting PPPO/DCM solutions of prescribed composition onto glass slides (50 mm diameter) and submerging them into heptane for 30 min. PPPO solutions (~ 1 mL) of 2-10 w/w% in DCM were allowed to evaporate to the desired concentration before non-solvent immersion (> 50 mL), resulting in films of several hundred μm, depending on concentration. These were then fully dried and imaged by SEM to characterise film morphology.

2.3. Scanning Electron Microscopy (SEM)

Sections of PPPO phase inverted films were mounted on carbon tape and coated with 15 nm of chromium before imaging with a LEO Gemini 1525 FEGSEM.

2

2.4. Differential Scanning Calorimetry (DSC)

A TA Instruments DSC (Q2000) was employed for samples in hermetically sealed aluminium pans (Tzero, codes: 901683.901 901684.901). Scans of neat polymer, kinetically arrested polymer rich phase, polymer films cast from solution (some vacuum dried, some containing solvent) and samples annealed in a Carbolite Gero were aquired at 10 °C (see figure S2 in supplementary information for temperature profiles). Degradation temperature of the polymer was determined by thermogravimetric analysis (see figure S3 in supplementary information).

2.5. Phase Mapping

2.5.1. Turbidity detection

The ternary phase diagram of PPPO/DCM/heptane was derived by visual examination, optical microscopy (Nikon Optiphot 2) and with dynamic light scattering (DLS, Malvern Zetasizer Nanoseries, angle: 173 °) to determine the turbidity onset of solutions upon the addition of heptane. Polymer in DCM solutions were prepared, at concentrations between 1 w/w% and 27 w/w%, increasing in increments of approximately 1 w/w%. Initially, heptane was added to 2 g of solution in 50 μL increments under agitation until cloudiness was observed (figure 2(a)). To increase measurement accuracy, this procedure was employed for DLS at concentrations of 2, 6, 10, 14, 16 and 18 w/w%, for 1.5 g solutions. Heptane was added again in 50 μL increments and agitated before each correlogram (figure 2(b) and (c)). For heptane concentrations greater than 40 w/w% a different approach was followed: mixtures of heptane:DCM between 40:60 w/w% and 100:0 w/w% were made in increments of 10 w/w%. PPPO solution of 0.005 w/w% was added dropwise until cloudiness was observed, and optical microscopy was used to confirm phase behaviour of selected compositions in one phase and two phase regions of the phase diagram.

2.5.2. Construction of tie lines

Demixed samples were centrifuged at 14500rpm for 15 minutes (Grant Microspin 12) in order to accelerate the coarsening process and facilitate the estimation of the volume fractions of PPPO-rich and -poor phases, which was carried out by a calibrated optical approach. The PPPO-poor phase has a negligible polymer content (estimated at less than 0.0025 w/w%) and was thus treated as a binary mixture of solvents, whose composition was estimated by ATR-FTIR from the calibration, following Figure 2(d) and (e)). The density (and thus mass) of the polymer-poor phase was then determined from a DCM:heptane calibration (Figure 2(f)) from which, imposing mass conservation, tie lines were constructed by connecting the compositions of the polymer-rich and -poor phases. The detailed procedure of tie line construction and a worked example, corresponding to arrows in Fig 2(e,f), are provided in Supplementary information (Section 1). The methodology used for this work is applicable to other similar polymer/solvent/nonsolvent systems.

2.6. Light transmission

Images were taken of a demixed sample in a 10 mm path length Hellma quartz cuvette back illuminated by a white light panel. The images were analysed using ImageJ to quantify the transmission of light through the sample and obtain a timeline of coarsening and kinetic arrest. Photographs were taken using a uEye UI-233x camera. Micrographs were taken of the interface between the coexisting phases of demixed solutions using a Basler acA1300 camera.

2.7. Wide and small angle X-ray scattering (WAXS/SAXS)

Kinetically arrested demixed samples were prepared from phase separated solutions: allowing the polymer rich phase to solidify, then siphoning off the solvent-rich phase and then drying the porous polymer material under vacuum.

SAXS data between 0.06 and 5° were aquired using a Rigaku Smartlab diffractometer with a 9kW anode Cu(K$_\alpha$) X-ray source, and for WAXS data , between 5 and 65°, with a Phillips Panalytical X'PERT PRO X-ray diffractometer with a Cu(K$_\alpha$) X-ray source.

2.8. Time Evolution

Selcted demixed solutions were prepared in two ways: Firstly, by the addition of heptane to a 4 w/w% solution of PPPO in DCM resulting in compositions at different quench depths into the two phase region (PPPO/DCM/heptane weight percent values are as follows: 2.7/67.7/29.6, 2.6/66.2/31.1 and 2.6/64.8/32.5). Secondly, two further samples were prepared along a tie line intersecting with the central 4% quench (PPPO/DCM/heptane weight percent values: 4.6/65.0/30.4 and 6.4/63.9/29.7). For all samples, the polymer rich bottom phase was allowed to stratify, and was then collected and placed on a glass cavity slide under a coverslip to prevent evaporation. Micrographs of the samples were taken using a Nikon Optiphot 2, at various times (up to 30 min) from demixing. Samples were further examined under cross-polarisers on an Olympus BX41M microscope over 4 hours during solidification.

3. Results and discussion

3.1. Phase mapping

Figure 3(a) shows a portion of the phase diagram (as depicted by the icon in the top left), highlighting individual compositions measured by turbidity. Green markers indicate the one-phase (1ϕ) region, and red indicates the two-phase (2ϕ) region. In general, increasing the weight percent of either polymer or heptane increases the likelihood of demixing; e.g. notice that polymer solutions of 1 w/w% require around 30 w/w % heptane to induce phase separation, whilst solutions of 10 w/w % PPPO require only 20 w/w % heptane. Demixing is observed due to difference in density and refractive index of the coexiting phases causing cloudiness and, in most cases, phase stratification (see figure 3(b)). The cloud point line measured by this method appears unexpectedly non-monotonic (see closed red circles on figure 3(a)) and requires further investigation [34], as it is likely a result of limited contrast close to the critical point.
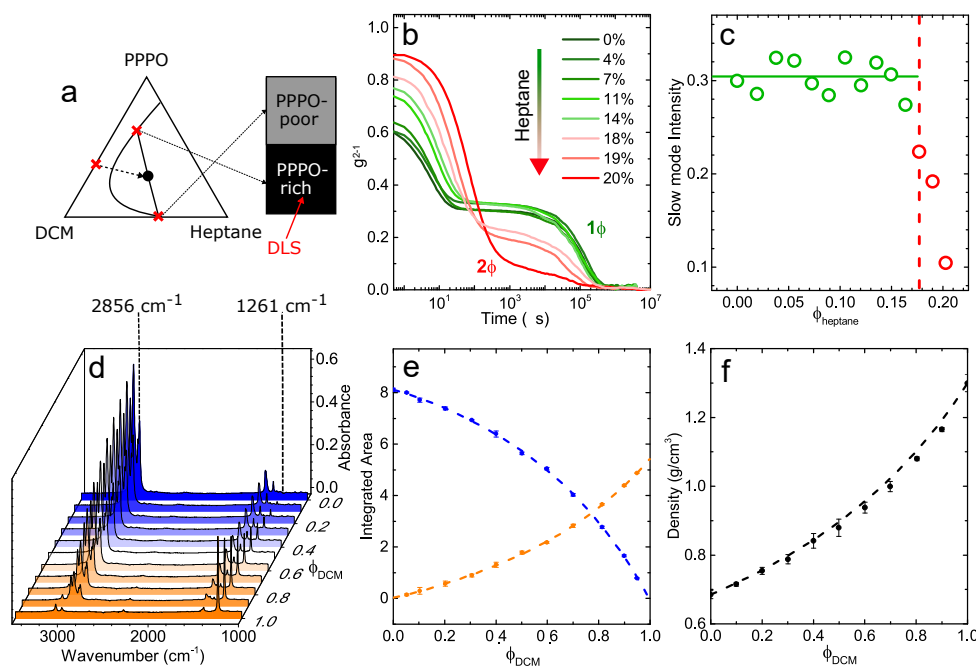
Figure 2: (a) Experimental procedure employed for phase mapping: solutions in the one-phase region were prepared from binary PPPO/DCM mixtures by incremental heptane addition and inspected visually, by optical microscopy and DLS; two-phase solutions were prepared individually and centrifuged and both coexisting phases analysed by ATR-FTIR and densitometry. (b) DLS data from illustrative 16% w/w PPPO/DCM solution upon addition of heptane; demixing is detected as the point of deviation from the double-exponential decay (red curves). (c) Dependence of the correlation coefficient of the slower decay with addition of heptane. (d) ATR-FTIR spectra of a range of DCM/heptane binary solutions; the characteristic heptane and DCM peaks at 2856 and 1261 cm^{-1}, respectively, were chosen for composition determination. (e) Calibration curves for the integrated area of the characteristic peaks at varying ratios of DCM/heptane. (f) Density calibration of the binary solvent mixtures. Arrows in (e,f) correspond to an example of composition estimation detailed in the text.

Phase separated mixtures close to the critical point will exhibit very similar composition, and likely will have similar refractive indices and density − thus limiting optical detection.

Measurements by DLS (open triangles on figure 3(a)) show good agreement with the turbidity measurements until around 12 w/w% (where this deviation occurs) and overall yields a smooth phase boundary, suggesting that DLS provides a more accurate turbidity detection. Figure 2 (b) demonstrates the typical shift of correlograms for a high PPPO concentration (16 w/w% in this instance) polymer solution as heptane is added.

DLS data at concentrations above the overlap concentration (c > c*), are expected to exhibit two modes, fast and slow, the former attributed to molecular diffusion, and the latter caused by a slow transient motion of gel networks and overlapping polymer chains within solution [35]. As heptane is added, and the liquid demixing line is approached, we observe that the amplitude of the fast mode increases and that of the slow mode decreases (figure 2(b)). Assigning these changes in DLS pattern to phase transitions gives the liquid demixing line (black open triangles on figure 3(a)). A similar technique was employed by van Hook *et al.* for pressure induced phase separation on polystyrene solutions [36].

Micrographs shown in figure 3(c) show solutions at selected compositions corresponding with blue circles displayed on figure 3(a), starting from the PPPO-DCM axis at 16 w/w% polymer (1), and adding heptane along a line that intersects with the apparent non-monotonic feature of the cloud point line. Images 1 and 2 were taken in the one-phase region, as determined by both DLS and visual examination. Image 4 is evidently the two-phase region, showing droplets of one phase suspended in the matrix of a second phase, characteristic of nucleation and growth. Pronounced phase contrast is expected at this deep quench. Image 3 is taken at a composition where turbidity is detected by DLS, but not visually corresponding to incipient phase separation and limited contrast, as expected for a shallow quench.

At compositions in the two phase region, phase separation is followed by kinetic arrest of the polymer rich phase to form a solid polymer (discussed in more detail in section 3.2). Previous studies of PPPO show that it can exhibit high crystallinity [14, 30], and DSC thermograms of neat polymer confirm this with a crystallisation peak at 336 °C (see figure 4(a) for films annealed for 2 h and 4 h). The glass transition temperature (Tg) can be seen for neat polymer at 228 °C, in line with Tg previously reported [14, 37]. The melting transition for neat PPPO is bimodal, and exhibits peaks at 423 and 445 °C, which suggests two different crystalline phases possibly the α and β modifications discussed by Boon and Magre [30]. This type of thermogram was seen by Wrasidlo, and was notable as the only one of the nine samples presented to exhibit this thermal behaviour - other samples exhibited sharp crystallisation (278 °C) and melting (497 °C) peaks [14]. This difference was attributed to a metastable crystalline phase (or phases) with two degrees of perfection induced by the increase in cooling rate; from 0.5
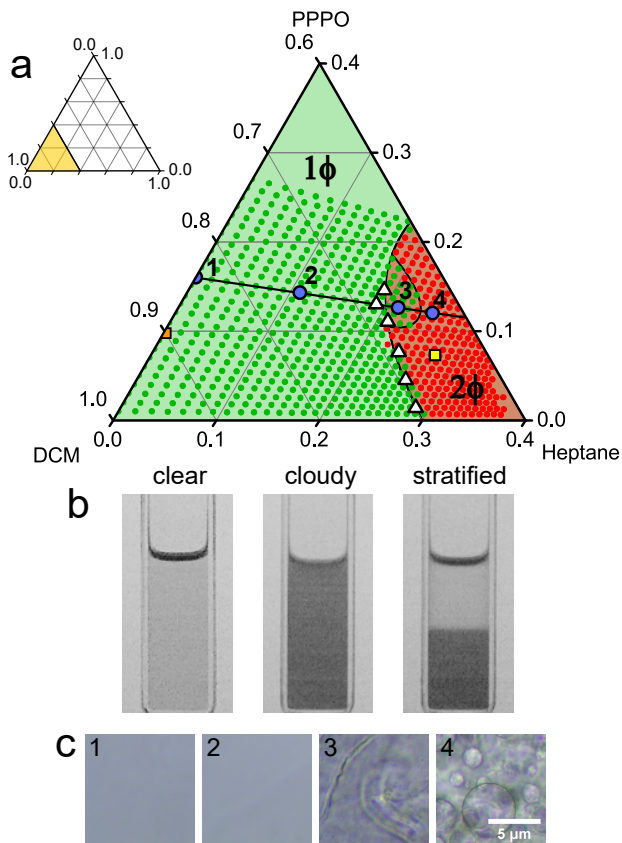
Figure 3: (a) Enlarged section of ternary phase diagram (shown by yellow high-lighted area of the triangular icon on the left). The one-phase region (1ϕ) is shown in green, and the two-phase region (2ϕ) in red; solid green and red circles represent compositions that are, respectively, visually clear and turbid; open triangles correspond to DLS phase boundary measurements. Blue circles are at compositions corresponding with images 1, 2, 3 and 4 shown in (b). (b) Optical micrographs of solutions corresponding to the blue circles on the phase diagram (a) (taken in 1 mm path length Hellma cells).(c) Illustrative one-phase solution (clear, 0.1:0.9 PPPO:DCM, corresponding to orange square shown in (a)) and a two phase sample (cloudy and stratified, 0.07:0.28:0.65 PPPO:DCM:Heptane, corresponding to yellow square shown in (a)) obtained by heptane addition.
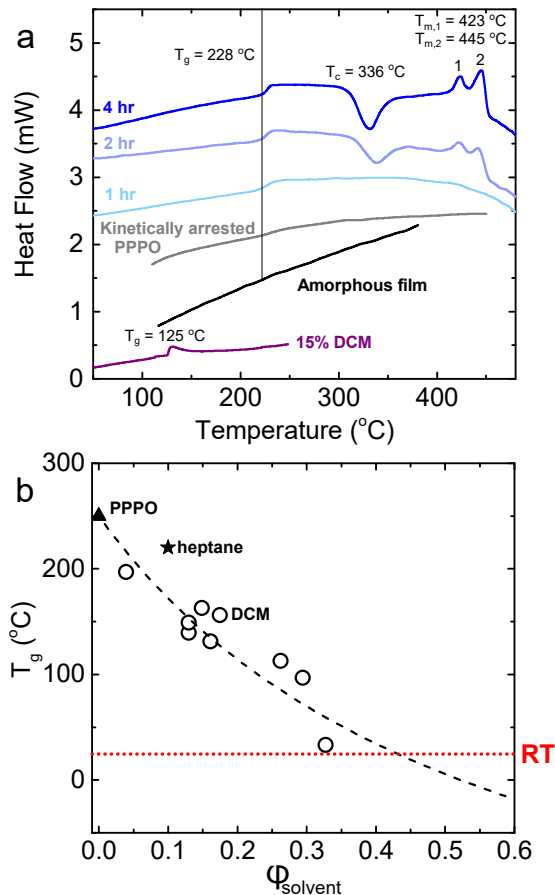

Figure 4: (a) DSC curves showing the glass transition temperature of neat PPPO (colour black), PPPO with 15 w/w% DCM (blue-grey), PPPO films annealed in a furnace at 400 °C at increasing times (blue, times labelled) in arbitrary units of heat flow. (b) Glass transition temperature variation as solvent content is increased, open circles represent samples with DCM and PPPO, black star represents sample of PPPO with maximum possible heptane swelling (10 w/w%), black cross shows the Tg of neat PPPO. The data has a Flory-Fox fit (black dashed line - see equation on graph) and the intersection with room temperature (RT) is shown (red dotted line), giving the solvent content required for PPPO to become glassy under these conditions.

to 5 °C/min. The cooling rate used in the current work was 10 °C/min, explaining why a single melting peak is not seen. The polymer begins to degrade at 480 °C (thermogravimetric analysis in Supplementary Figure S2). Thermograms of the kinetically arrested phase separated polymer (figure 4(a) grey curve) reveal that this phase solidifies in a glassy state, thus processing is required for the polymer to crystallise. The high crystallinity of PPPO is relevant to its final morphology, and therefore applications; The crystal void size has been previously reported to be 4.8 Å by Alentiev *et al.* [28], which is large enough to accommodate small volatiles like CO_2. Figure 4(a) shows that films annealed in a furnace at 400 °C for 2 hr and 4 hr show crystal features (bimodal melting peaks) as well as a (single) glass transition. Films that have solvent content and are not annealed show only a glass transition temperature (see figure 4(a)) and are therefore amorphous. Heating over a prolonged (at least 2h) time above the crystallisation temperature is re-

quired to induce crystallisation. Solvent can act as a plasticiser in polymer films and lower the various transition temperatures by increasing chain mobility and thus lowering energy requirements [38]. It follows that during phase separation when a polymer rich phase is formed, kinetic arrest may occur at significant solvent content in high T_g PPPO. Figure 4(b) shows the change T_g as a function of DCM content, the curve follows a Flory-Fox relation $\frac{1}{T_g} = \frac{\phi_P}{T_{g,P}} + \frac{\phi_S}{T_{g,S}}$ [39] (displayed as dashed line on figure). The T_g of PPPO is similarly decreased by heptane (black star on figure), however the temperature drop is less as heptane is a poor solvent for PPPO.

From the fit, Tg intersects with room temperature at 40 w/w% solvent content (plus or minus 10% due to error), therefore we can expect that demixed polymer rich phases become kinetically arrested at around 30-50 w/w% polymer, upon reaching the glass transition. The intersection of this line with the thermodynamic phase boundary of the ternary system, suggests that the polymer-rich phase is kinetically arrested before
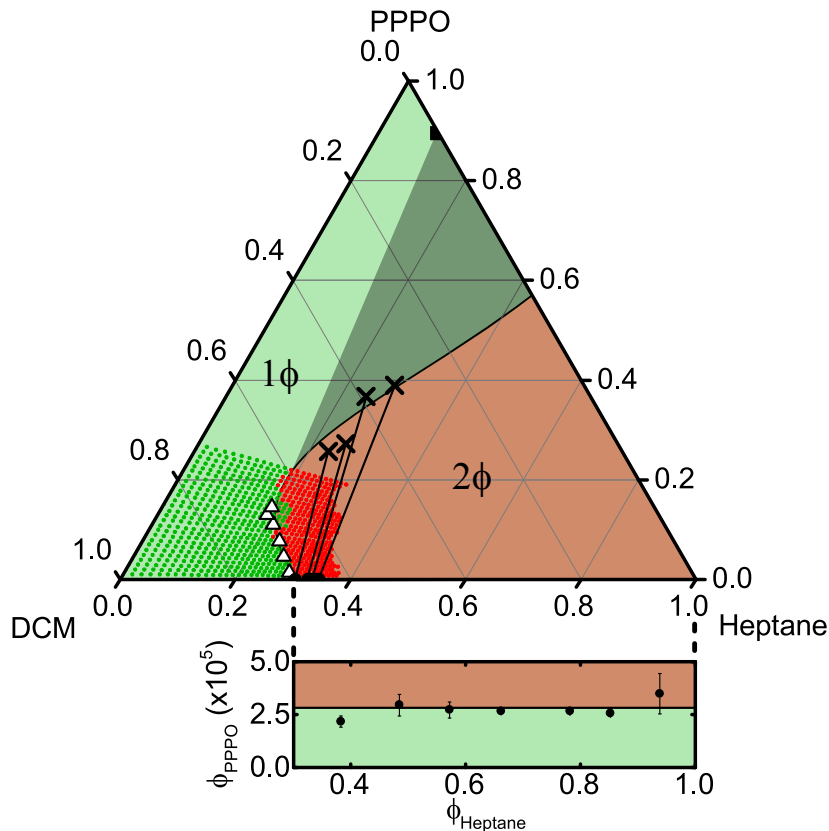
Figure 5: Experimentally measured full ternary phase diagram for PPPO/DCM/heptane, showing the one-phase region (1ϕ) in green, and the two-phase region (2ϕ) in red; solid green and red circles represent compositions that are, respectively, visually clear and turbid; open triangles correspond to DLS phase boundary measurements. Below shows an enlarged section of the phase boundary along the DCM:heptane binary axis obtained by turbidity upon PPPO addition, this estimates an upper concentration for PPPO in the polymer-poor phase.

reaching equilibrium, as shown in figure 5.

The figure shows the entire ternary phase diagram, including an enlargement of the DCM-heptane axis. Heptane and DCM are miscible in all proportions, therefore we would expect the miscible region to extend along the bottom axis at a sufficiently low polymer content [40]. For solutions containing more than 30 w/w% heptane, turbidity was seen at average PPPO concentrations of 0.0025 w/w%, exhibiting the polymers incompatibility with heptane, despite the full solvent miscibility. We use this feature of the phase diagram to derive tie-lines using the method outlined in the worked example (section 1 in SI). Measurements on this system are limited by polymer kinetic arrest above concentrations of 27 w/w%, meaning heptane cannot be mixed into solutions above this weight percent. The construction of tie lines afford a means to extend the phase boundary into this experimentally inaccessible region.

The estimated tie-lines are shown in black on figure 5, and polymer-rich phase compositions for these demixed solutions are shown using a black cross. These composition have a polymer content of around 30-40% which, as previously discussed, is around the region we would expect kinetic arrest to take place (figure 4(b)). By extrapolating the phase boundary measured by turbidity to intersect with these tie-lines (red shaded region of figure 5), we obtain a kinetic, rather than a phase, bound-

ary. The dark green area shows a tentative theoretical thermodynamic phase boundary, by extrapolating the measured phase boundary, so it intersects with the point of maximum miscibility of PPPO and heptane on the PPPO-heptane axis (10 w/w% PPPO, 90 w/w% heptane - this point was independently measured experimentally, shown as black square on figure).

3.2. Demixing and solidification

The transmission of light through a quiescent demixed sample allows for the evolution of demixing and solidification to be followed in time. Figure 6(a) shows a schematic set up of this experiment, measuring the average light transmission through a demixed sample in a glass cuvette across the cuvette height (z (mm)). The sample is a mixture of two liquids, until the polymer-rich phase solidifies.

Figure 6(b) shows a selection of images corresponding to Figure 6(c) which depicts the average light transmission through the top (polymer-poor phase averaged across the cuvette at z ≥ 12 mm) and bottom (polymer-rich phase averaged across the cuvette at z ≤ 10 mm). The process can be classified in three stages over the measured time period of 13 h, according to their on light transmission profile. Firstly, stratification occurs within the first minute of demixing. The transmission through the cuvette is initially uniform in z, before the denser
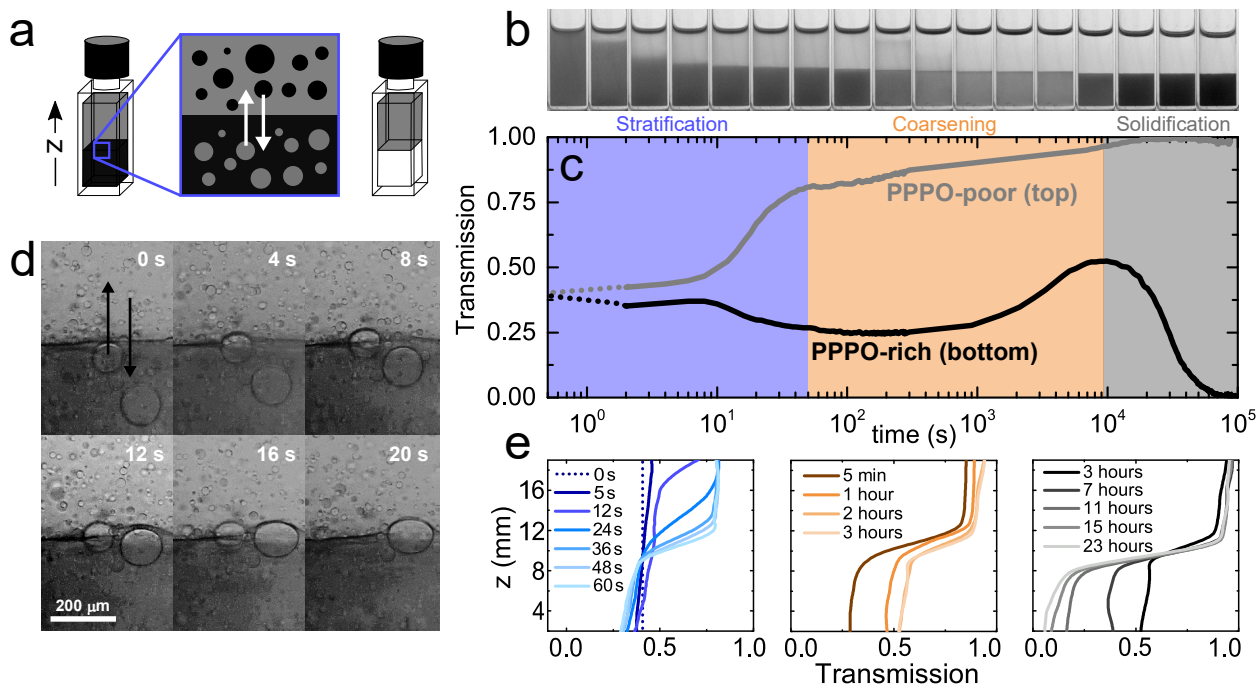
Figure 6: (a) Selected optical images of the demixing process of a 10% PPPO/DCM solution upon addition of heptane (7.2%/65.2%/27.6% PPPO/DCM/heptane), from which three distinct stages can be identified: 1) stratification, 2) coarsening, and 3) solidification. (b) Evolution of the average transmission with time for the top, polymer-poor phase, (grey) and the bottom, polymer-rich phase (black). (c) Magnified optical images of the interface between coexisting phases of the solution within the coarsening stage (time rescaled to this stage). (d) Evolution of optical transmission as a function of z (cuvette height) and time during the 3 stages identified. (e) Schematic of coarsening process and density-driven flows at the interface, and eventual solidification of the polymer-rich phase; z is defined from the bottom of the cuvette.

polymer-rich phase and the less dense polymer-lean phase segregate to the bottom and top, driven by buoyancy. At the end of this stage, the interface between the bulk phases is now distinct, while each phase still contains droplets of the other.

During the second stage, termed coarsening, smaller droplets of each phase coalesce, which reduces the turbidity and increases light transmission in both the top and bottom phases (figure 6 (c) and corresponding images of the cuvette in (b)). This coarsening process takes place over a long period of time (approx. 4 hrs) and is assisted by density driven flows. Figure 6(d) shows a magnified side-on view of a demixed and stratified sample at the interface between the two demixing liquids, with upward and downward droplet motion due to density driven flows. The solvent rich droplets grow in size by coalescence of smaller droplets whilst travelling up towards the interface and then fuse with the polymer lean phase ($\Delta t = 16 - 18$ s). Polymer rich droplets travelling downwards are much smaller, as any large droplets will have already stratified given their higher mass.

Given that motion of the droplets is primarily due to gravity, the ratios of viscosity (ρ) of the two phases can be estimated using Stokes Law: $F_g = (\rho_d - \rho_f)g\frac{4}{3}\pi R^3$. Where F is the force due to gravity and R is the droplet radius. Therefore, the velocity (v) of droplets is expressed as: $v = \frac{2}{9}\frac{(\rho_d-\rho_f)}{\mu}gR^2$, and the ratio of the viscosity of the two phases can be estimated as $\frac{\mu_S}{\mu_P} = -\frac{v_l R_R^2}{v_R R_l^2} = 8.6 \pm 0.1$. Since the composition of the top phase has been shown to contain trace polymer amounts, the

viscosity of the polymer lean phase μ_S can be approximated by the pure solvent mixture. The viscosities of heptane and DCM are respectively, 0.38 and 0.41 mPas (at 25°C), the viscosity of the mixture at this composition can be reasonably estimated by the weighted average at 0.40 mPas. The viscosity of the polymer-rich phase (i.e. the matrix of the droplets within the bottom phase) can thus be readily estimated at 3.4 mPas. We note however that this estimate applies within approximately 1 min of non-solvent addition, upon completion of the stratification stage, and that this viscosity will increase over time during the coarsening stage, until kinetic arrest (solidification stage) where it diverges, still trapping polymer-lean droplets.

Solidification is the final stage. The polymer rich phase densifies as it coarsens, to a point at which its composition approaches the glass transition at room temperature (see figure 4(b)), and it kinetically arrests. During the solidification of the bottom phase, the transmission decreases (figure 6 (c) and corresponding images in (b)), while the transmission of the top phase increases further. This solid polymer phase is amorphous and the low light transmission is thus due to scattering of the demixed structure (instead of, for instance, crystallisation). The evolution of optical transmission as a function of height, z, and time for the three stages is shown in figure 6(e). Evidently, the timescales associated with stage each are *extensive* quantities, i.e. depend on sample volume and, in particular, height. We have therefore carried out a series of measurements varying sample volume, which enabled us to conclude that: the lateral dimensions (xy) are inconsequential (except for very low
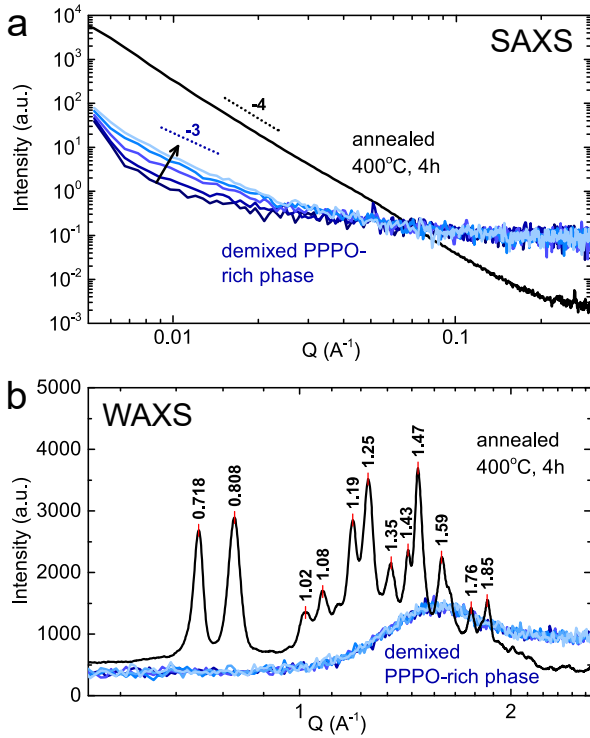
7

Figure 7: (a) SAXS data of the polymer-rich phase (estimated at 25.9%/50.8%/23.3% PPPO/DCM/heptane from tie-line) obtained from the demixing of a ternary mixture (7.2%/65.2%/27.6% PPPO/DCM/heptane) as a function of time (4, 8, 12, 16, 20h), including representative power laws. SAXS data for a solid sample annealed in a furnace at 400°C are included for comparison. (b) Corresponding WAXS data for this sample as a function of time exhibiting an amorphous structure that is unchanged with time. The crystalline structure of a sample annealed in a furnace at 400°C is also shown (black).

sample heights, commensurate with the curvature of the liquid meniscus); the stratification kinetics were estimated by the timescale τ for the interface between phases to drop from the initial sample height to its asymptotic value, Δz. Experimentally, we find $\tau = 0.071\Delta z + 7.4$ at this ternary composition and room temperature (see figure 4 in SI). Interestingly, the (much longer) timescales associated with coarsening and solidification are largely unchanged for the conditions investigated (since τ is much shorter than the time to solidification).

3.3. Time evolution of structure

3.3.1. Crystallisation

Upon demixing and stratification, the PPPO-rich phase was analysed with a combination of SAXS and WAXS. A ternary mixture of 7.2%/65.2%/27.6% PPPO/DCM/heptane was allowed to demix and stratify, after which the PPPO-rich phase was measured over time (up to 20h). The composition of this phase can be estimated as 25.9%/50.8%/23.3% PPPO/DCM/heptane from tie line construction reported earlier. The SAXS/WAXS profiles (blue lines), shown in Figure 7, indicate the formation of an amorphous polymer phase with a SAXS profile increasing gradually over time (Figure 7(a), exhibiting $I \sim I(0)q^{-3}$ at low q for nearly one decade in q. It is significant that crystallinity did not arise upon demixing at room

temperature under any of the conditions investigated; equally, the large lengthscale evolution over $\sim$ 1 day is characteristic of asymptotically slow dynamics near T_g. We attribute no particular significance to the -3 power law given the relatively narrow Q-range where it is observed; however, it would be compatible with the scattering expected from a rough surface fractal, as might be expected from pores or polymer-rich cluster aggregation [41]. These scattering objects are evidently larger than $\sim$ 100 nm (corresponding to $q_{min} \approx 2\pi/0.006\text{Å}^{-1}$), and indeed visible by optical microscopy. No structural (e.g. spinodal) peak is visible in the data.

By contrast, a PPPO film (solution cast from DCM) and then annealed under N_2 at 400°C, between T_c and T_m exhibits a clear $I \simeq I(0)q^{-4}$ dependence in the SAXS data expected for smooth surface fractals, following the well-known Porod law. WAXS reveals pronounced structural peaks, as expected for this highly crystalline polymer [30]. Previous studies reported the formation two crystalline structures: α and β [30]. Figure 7(b) shows the x-ray diffraction pattern of the annealed crystalline PPPO (black), with indexed peaks, which we find to correspond to the α-polymorph. The corresponding unit cell is tetragonal (a = b = 12.51 Å, c = 17.08 Å), containing eight monomeric units, and two molecular chains pass through each unit cell in a helical conformation, as reported by Boon and Magre [30].

3.3.2. Bulk solution morphology

We next consider how solution thermodynamics impacts the resulting phase morphology, in terms of the quench depth into the two phase region, and its evolution in time. Figure 8(a) describes the experimental procedure and the portion of the two-phase region examined, relating to micrographs of the polymer-rich phase show in figures 8(b) (along a tie-line) and (c) at increasing quench depths. Under these conditions, nucleation and growth appears to be the dominant demixing mechanism in this composition range. Coarsening was evaluated in terms of the evolution of the characteristic domain site with respect to time (see figure 8 (d)). The growth rate can be expressed by a 1/3 power law relationship, $R \propto t^{1/3}$, typical for Brownian coalescence (as well as evaporation-condensation) mechanisms, the centre of mass movement supports the former.

The effect of quench depth is shown in figure 8 (c). As expected, the deeper the quench the larger the radii of the droplets, at a given time in solution, due to the increase in thermodynamic driving force and thus the coarsening rate. At sufficiently long times, morphological coarsening is expected to slow down due to the increased viscosity of the polymer rich phase, and eventually become kinetically arrested near the glass transition (figure 4(b)). Figure 8 (b) follows compositions along a tie line, with increasing initial polymer concentration. Considering that points along a tie-line must result in different volumes of the same phase compositions, one might expect droplet size and growth rate to remain the same. Instead, droplet size was found to increase with increasing polymer composition, along the tie-line. This can be rationalised by the asymmetry of volume fractions of the demixed phases near the phase boundaries, which decreases and the polymer composition increases and thus results in larger phase sizes upon coarsening.
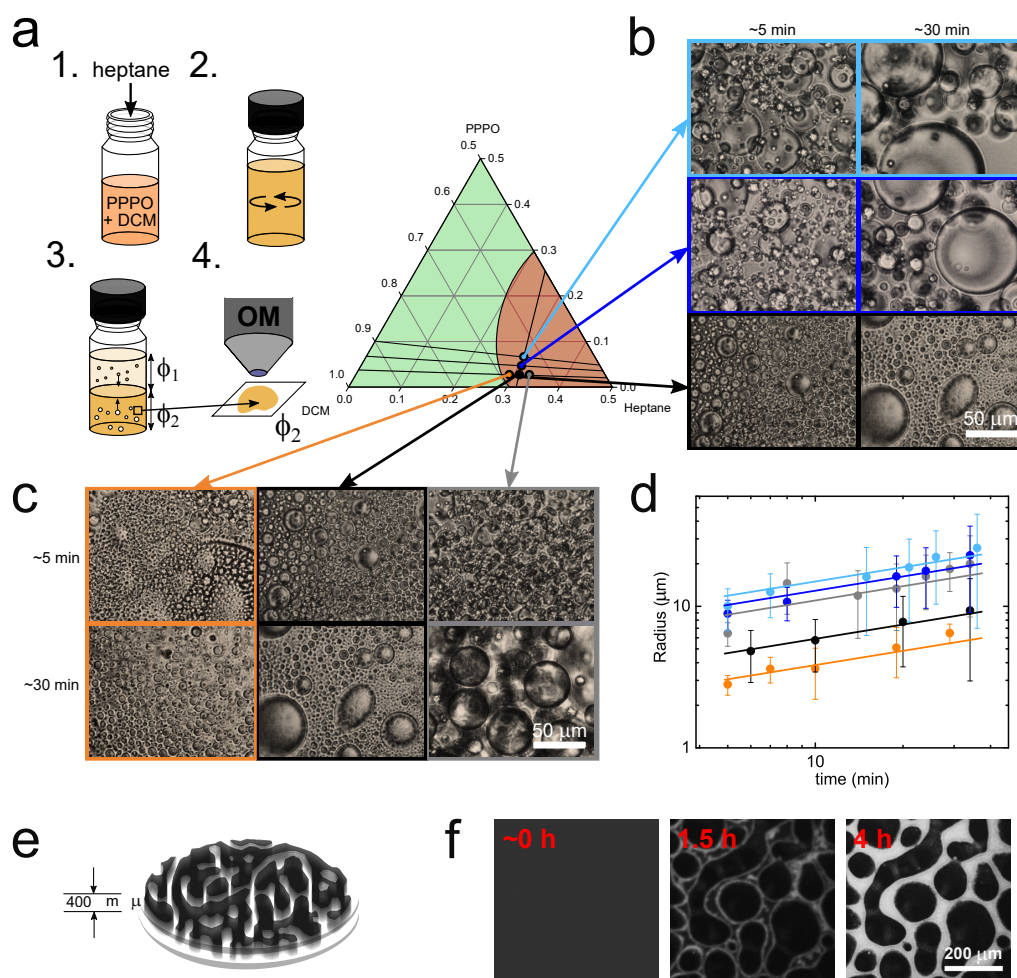
Figure 8: Illustrative demixed bulk solution morphologies obtained by 2ϕ quenches from binary PPPO/DCM solutions. (a) Schematic experimental procedure showing the addition of heptane, mixing, stratification and optical microscopy of the polymer rich phase (ϕ_2), as well as the enlarged section of the phase diagram with the representative compositions investigated with colours corresponding to the micrographs shown in (b) and (c). (b) Optical microscopy images of the demixed solutions along the tieline shown by black, blue and purple points on (a), and (c) of quenches of varying depth from a 5% PPPO/DCM initial solution by heptane addition, shown by the orange, black and grey points on (a). (d) Corresponding droplet size as a function of time for the illustrative quenches, showing a 1/3 power law growth rate (e) Schematic showing the experimental conditions for (f). (f) Micrographs taken of a demixed sample between two glass slides under cross polarisers, showing the evolution of structure under confinement during solidification.

Spinodal decomposition was not observed in solution for quenches from binary (PPPO/DCM) to ternary mixtures by heptane addition. However, it was found under slow evaporation conditions where the overall composition is not constant, as the higher volatility of DCM leads to a curved composition pathway (figure 8(e) and (f)). It is possible that the spinodal region is narrow at room temperature for this system, or that its characteristic lengthscale is below that accessible by optical microscopy and rapidly evolves into a droplet morphology.

3.3.3. Porous Film Formation

Figure 9 illustrates the potential to harness the ternary phase behaviour to design specific morphological features, relevant to porous membranes. Figure 9(a) depicts the film formation by non-solvent immersion, and (b) shows the overall composition pathways of the films from the initial PPPO/DCM (markers) into a large heptane excess. The shaded regions on figure 9(b)

approximate the resultant morphologies of films prepared from these compositions, with colours corresponding to the SEM images seen in figure 9(c), with nodular (yellow), bicontinuous (teal) and cellular (light red) morphologies [42]. Nodular structures are obtained from the films with the lowest polymer content (2%, 5% and the top side of the 10% film). This is likely due to a combination of their low viscosity and low volume fraction of the polymer-rich phase, resulting in the kinetic arrest and agglomeration of the 'nodules' shown. We note that nodules are only present on the top side of the 10% film, which is in immediate contact with the non-solvent, resulting in an asymmetric membrane, as the bottom surface is (impermeable) glass. By contrast, bicontinuous structures are found at 10 and 15% (bottom surface) suggesting that these films were arrested in the spinodal region of the phase diagram, indicative of the fine balance between thermodynamics, dynamic composition profile and kinetic arrest required to obtain an interconnected
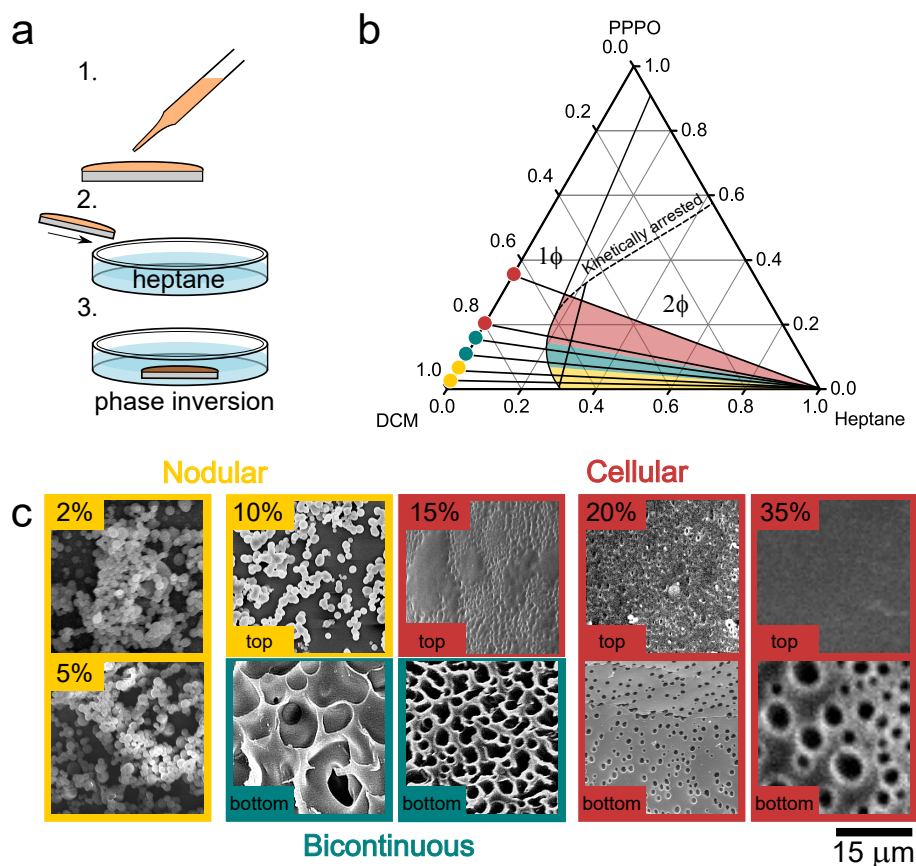
Figure 9: (a) Schematic depicting film formation through phase inversion by drop casting a PPPO/DCM film onto glass and subsequent immersion into an excess of non-solvent heptane. (b) Phase behaviour with solid lines indicating the overall composition pathways induced by demixing with a large excess of heptane. Coloured circles show the initial film compositions and shaded coloured sections correspond to the resulting morphologies (nodular, bicontinuous and cellular) as seen by SEM in (c). A tie-line is also shown to rationalise the relative volume fractions of the polymer rich and poor phases. (c) SEM images of the resulting films at 2, 5, 10, 15, 20 and 35% showing the top and bottom surfaces (except for 2 and 5%, for which only top is shown). The scale bar is 15 μm.

morphology. The smaller pore lengthscale in films cast at 15% is likely due to the larger quench into the unstable region, and higher volume fraction of the polymer-rich phase. A cellular (or inverted nodular) morphology is obtained from films of higher polymer content (20 and 35%), likely resulting from morphologies arrested within the metastable region, where the PPPO-rich phase is now the majority phase, and the circular pores being generated upon evaporation of the solvent-rich droplet phase. Larger pore sizes seen for the 35% film (bottom surface) which is likely due to the slower inversion process at higher polymer content and thus longer coarsening times available before kinetic arrest.

4. Conclusions

The ternary phase diagram of poly(2,6-diphenyl-p-phenylene oxide) in mixtures of dichloromethane (solvent) and heptane (nonsolvent) was measured for the first time, employing a combination of methods to detect the liquid-liquid demixing line, namely, optical detection, microscopy, and dynamic light scattering (DLS). We adopted a sequential procedure for the de-

termination of tie-lines based on the attenuated total reflection (ATR) Fourier transform infrared (FTIR) spectroscopy measurement of the polymer-poor phase. The tie-lines defined by this method allow us to extrapolate the measured phase boundary into the concentrated polymer region of the ternary diagram, to establish demixing pathway.

In the two phase region, the demixing process can be rationalised in terms of three stages: (1) stratification, (2) coarsening and (3) solidification, each of these with distinct kinetics and features. Large density differences in the polymer-rich and poor phases lead to a rapid stratification, followed by a much slower coarsening process, assisted by buoyancy-driven flows.

Densification of the polymer rich phase finally affects solidification by kinetic arrest, resulting in an amorphous glass, characterised by small angle x-ray scattering (SAXS), wide angle x-ray scattering (WAXS) and differential scanning calorimetry (DSC). The intersection between the phase boundary and T_g of the polymer-rich phase was experimentally measured. The amorphous polymer glass formed via this process can crystallise under high temperature conditions (above 330 °C). Isothermal annealing, carried out under nitrogen atmosphere,

yields crystalline PPPO with α-structure, in line with previous observations [30].

We demonstrate how these thermodynamic data can be used to controllably generate porous polymeric microstructures of prescribed pore sizes and morphologies, by varying the quench depth, initial polymer composition and evaluating the evolution of these structures with respect to time. In general, increasing the depth of the quench increases the driving force and thus the rate of coarsening. Droplets radius increases with time with a 1/3 power law growth rate, as expected from diffusive droplet growth mechanics [43]. The morphology type corresponds qualitatively with the expected region of the phase diagram, and nodular, bicontinuous and cellular structures are obtained in non-solvent immersed films, whose cross-section then becomes asymmetric due to the directionality of the phase inversion process.

We find that liquid-liquid phase separation can only produce an amorphous polymer-rich phase due to kinetic arrest, at all conditions investigated. Crystallinity can be induced, after demixing, by annealing above T_c. Our results are relevant to the predictive design of nano/microporous PPPO polymer materials, membranes and scaffolds.

Acknowledgements

References

[1] E. Aram, S. Mehdipour-Ataei, A review on the micro-and nanoporous polymeric foams: Preparation and properties, International Journal of Polymeric Materials and Polymeric Biomaterials 65 (7) (2016) 358–375. doi:https://doi.org/10.1080/00914037.2015.1129948.

[2] P. van de Witte, P. Dijkstra, J. van den Berg, J. Feijen, Phase separation processes in polymer solutions in relation to membrane formation, Journal of Membrane Science 117 (1-2) (1996) 1–31. doi:https://doi.org/10.1016/0376-7388(96)00088-9.

[3] L. Robeson, Polymer Membranes, in: Polymer Science: A Comprehensive Reference, Elsevier, 2012, pp. 325–347. doi:https://doi.org/10.1016/B978-0-444-53349-4.00211-9.

[4] G. R. Guillen, Y. Pan, M. Li, E. M. V. Hoek, Preparation and Characterization of Membranes Formed by Nonsolvent Induced Phase Separation: A Review, Ind. Eng. Chem. Res 50 (7) (2011) 3798–3817. doi:https://doi.org/10.1021/ie101928r.

[5] L. H. Sperling, Introduction to Physical Polymer Science, 4th Edition, Wiley, Hoboken, New Jersey, 2006. doi:https://doi.org/10.1002/0471757128.

[6] H. Strathmann, K. Kock, The formation mechanism of phase inversion membranes, Desalination 21 (3) (1977) 241–255. doi:https://doi.org/10.1016/S0011-9164(00)88244-2.

[7] T. Ishigami, K. Nakatsuka, Y. Ohmukai, E. Kamio, T. Maruyama, H. Matsuyama, Solidification characteristics of polymer solution during polyvinylidene fluoride membrane preparation by nonsolvent-induced phase separation, Journal of Membrane Science 438 (2013) 77–82. doi:https://doi.org/10.1016/j.memsci.2013.03.011.

[8] H. Strathmann, K. Kock, P. Amar, R. Baker, The formation mechanism of asymmetric membranes, Desalination 16 (2) (1975) 179–203. doi:https://doi.org/10.1016/S0011-9164(00)82092-5.

[9] C. A. Smolders, A. J. Reuvers, R. M. Boom, I. M. Wienk, Microstructures in phase-inversion membranes. Part 1. Formation of macrovoids, Journal of Membrane Sctence 73 (2-3) (1992) 259–275. doi:https://doi.org/10.1016/0376-7388(92)80134-6.

[10] C. E. Udoh, V. Garbin, J. T. Cabral, Microporous Polymer Particles via Phase Inversion in Microfluidics: Impact of Nonsolvent Quality, Langmuir 32 (32) (2016) 8131–8140. doi:10.1021/acs.langmuir.6b01799.

[11] S. Bonyadi, M. Mackley, The development of novel micro-capillary film membranes, Journal of Membrane Science 389 (2011) 137–147. doi:https://doi.org/10.1016/j.memsci.2011.10.023.

[12] P. J. Akers, G. Allen, M. J. Bethell, The Unperturbed Dimensions of Poly-(2,6-dimethyl-l,4-phenylene oxide) and Poly(2,6-diphenyl-l, 4-phenylene oxide), Polymer 9 (1968) 575–584. doi:https://doi.org/10.1016/0032-3861(68)90074-8.

[13] A. R. Shultz, Unperturbed dimensions of poly(2-methyl-6-phenyl-1,4-phenylene oxide) and poly(2,6-diphenyl-1,4-phenylene oxide) chains, Journal of Polymer Science Part A-2: Polymer Physics 8 (6) (1970) 883–891. doi:https://doi.org/10.1002/pol.1970.160080605.

[14] W. Wrasidlo, Transitions and relaxations in poly(1,4-phenylene ether), Journal of Polymer Science Part A-2: Polymer Physics 10 (9) (1971) 1719–1729. doi:https://doi.org/10.1002/pol.1972.160100908.

[15] A. S. Hay, Poly(2,6-diphenyl-l,4-phenylene oxide), Macromolecules 2 (1) (1969) 107–108. doi:https://doi.org/10.1021/ma60007a022.

[16] A. Hay, N. Y. Schenectady, Process of Making Poly-(2,6-diaryl-1,4-phenylene ethers) (1969).
URL https://patents.google.com/patent/US3432466A/en

[17] J. Vermeer, W. B. Kema, J. Bussink, H. Brakel, Tenax, a new low-loss high-temperature resistant synthetic paper for EHV cables and other electrical equipment, in: Conference on Electrical Insulation & Dielectric Phenomena - Annual Report 1970, IEEE, 1970, pp. 56–63. doi:https://doi.org/10.1109/CEIDP.1970.7725106.

[18] A. S. Hay, 2,6-Diarylphenols (1969).
URL https://patents.google.com/patent/US3481990

[19] A. S. Hay, R. F. Clark, Poly (2,6-diaryl-1,4-phenylene oxides), Macromolecules 3 (5) (1970) 533–535. doi:https://doi.org/10.1021/ma60017a012.

[20] R. van Wijk, The Use of Poly-Para-2, 6-Diphenyl-Phenylene Oxide as a Porous Polymer in Gas Chromatography, Journal of Chromatographic Science 8 (7) (1970) 418–420. doi:https://doi.org/10.1093/chromsci/8.7.418.

[21] E. D. Pellizzari, J. E. Bunch, R. E. Berkley, J. McRae, Collection and Analysis of Trace Organic Vapor Pollutants in Ambient Atmospheres. the Performance of a Tenax gc Cartridge Sampler for Hazardous Vapors, Analytical Letters 9 (1) (1976) 45–63. doi:https://doi.org/10.1080/00032717608059080.

[22] R. H. Brown, C. J. Purnell, Collection and analysis of trace organic vapour pollutants in ambient atmospheres: the performance of a Tenax-GC adsorbent tube, Journal of Chromatography 178 (1979) 79–90. doi:https://doi.org/10.1016/S0021-9673(00)89698-3.

[23] S. B. Hawthorne, D. J. Miller, Extraction and Recovery of Organic Pollutants from Environmental Solids and Tenax-GC Using Supercritical CO2, Journal of Chromatographic Science 24 (6) (1986) 258–264. doi:https://doi.org/10.1093/chromsci/24.6.258.

[24] V. Camel, M. Caude, Trace enrichment methods for the determination of organic pollutants in ambient air, Journal of Chromatography A 710 (1) (1995) 3–19. doi:https://doi.org/10.1016/0021-9673(95)00080-7.

[25] M. Harper, Sorbent trapping of volatile organic compounds from air, Journal of Chromatography A 885 (1-2) (2000) 129–151. doi:https://doi.org/10.1016/S0021-9673(00)00363-0.

[26] B. Alfeeli, L. T. Taylor, M. Agah, Evaluation of Tenax TA thin films as adsorbent material for micro preconcentration applications, Microchemical Journal 95 (2) (2010) 259–267. doi:https://doi.org/10.1016/j.microc.2009.12.011.

[27] B. Alfeeli, V. Jain, R. K. Johnson, F. L. Beyer, J. R. Heflin, M. Agah, Characterization of poly(2,6-diphenyl-p-phenylene oxide) films as adsorbent for microfabricated preconcentrators, Microchemical Journal 98 (2) (2011) 240–245. doi:https://doi.org/10.1016/j.microc.2011.02.006.

[28] A. Alentiev, E. Drioli, M. Gokzhaev, G. Golemme, O. Ilinich, A. Lap-

kin, V. Volkov, Y. Yampolskii, Gas permeation properties of phenylene oxide polymers, Journal of Membrane Science 138 (1) (1998) 99–107. doi:https://doi.org/10.1016/S0376-7388(97)00219-6.

[29] O. Ilinitch, V. Fenelonov, A. Lapkin, L. Okkel, V. Terskikh, K. Zamaraev, Intrinsic microporosity and gas transport in polyphenylene oxide polymers, Microporous and Mesoporous Materials 31 (1-2) (1999) 97–110. doi:https://doi.org/10.1016/S1387-1811(99)00060-8.

[30] J. Boon, E. P. Magré, Structural studies of crystalline poly(pphenylene oxides) I. Poly(pphenylene oxide), Die Makromolekulare Chemie 126 (1) (1969) 130–138. doi:https://doi.org/10.1002/macp.1969.021260115.

[31] K. Sakodynskii, L. Panina, N. Klinskaya, A study of some properties of Tenax, a porous polymer sorbent, Chromatographia 7 (7) (1974) 339–344. doi:https://doi.org/10.1007/BF02269347.

[32] M. Aguilar-Vega, D. R. Paul, Gas transport properties of polyphenylene ethers, Journal of Polymer Science Part B: Polymer Physics 31 (11) (1993) 1577–1589. doi:https://doi.org/10.1002/polb.1993.090311114.

[33] R. H. Perry, D. W. Green, Perry's chemical engineers' handbook, 8th Edition, McGraw-Hill, New York, 2008.

[34] H. Okamoto, T. B. Massalski, Thermodynamically Improbable Phase Diagrams, Journal of Phase Equilibria 12 (2) (1991) 148–168. doi:https://doi.org/10.1007/BF02645711.

[35] E. Saldivar-Guerra, E. Vivaldo-Lima, Handbook of Polymer Synthesis, Characterization, and Processing, Wiley, 2013. doi:https://doi.org/10.1002/9781118480793.

[36] W. A. Van Hook, H. Wilczura, L. P. N. Rebelo, Dynamic Light Scattering of Polymer/Solvent Solutions Under Pressure. Near-Critical Demixing (0.1 ¡ P/MPa ¡ 200) for Polystyrene/ Cyclohexane and Polystyrene/Methylcyclohexane, Macromolecules 32 (1999) 7299–7311. doi:https://doi.org/10.1021/ma990238b.

[37] A. S. Hay, J. Y. Guttman, J. E. Guillet, P. Blais, R. St John, Poly(2,6-diphenyl-l,4-phenylene oxide), Tech. Rep. 1 (1969). doi:https://doi.org/10.1021/ma60007a022.

[38] H. Berghmans, F. Govaerts, N. Overbergh, Gelation and crystallization of poly(ethylene terephthalate-co-isophthalate), Journal of Polymer Science: Polymer Physics Edition 17 (7) (1979) 1251–1267. doi:https://doi.org/10.1002/pol.1979.180170709.

[39] T. G. Fox, P. J. Flory, Second-Order Transition Temperatures and Related Properties of Polystyrene. I. Influence of Molecular Weight, Journal of Applied Physics 21 (1950) 581–591. doi:https://doi.org/10.1063/1.1699711.

[40] D. R. F. West, N. Saunders, Ternary Phase Diagrams in Materials Science, 3rd Edition, Maney Publishing, London, 2002. doi:https://doi.org/10.4324/9781315087399.

[41] J. Teixema, Small-Angle Scattering by Fractal Systems, Tech. rep. (1988).

[42] A. Venault, Y. Chang, D.-M. Wang, D. Bouyer, Polymer Reviews A Review on Polymeric Membranes and Hydrogels Prepared by Vapor-Induced Phase Separation Process) A Review on Polymeric Membranes and Hydrogels Prepared by Vapor-Induced Phase Separation Process, Polymer Reviews, 53:4, 568-626, A Review on, Polymer Reviews 53 (2013) 568–626. doi:10.1080/15583724.2013.828750.

[43] I. M. Lifshitz, V. V. Slyozov, The kinetics of precipitation from supersaturated solid solutions, J. Phys. Chem. Solids Pergamon Press 19 (2) (1961) 35–50. doi:https://doi.org/10.1016/0022-3697(61)90054-3.